THE JOURNAL OF PHYSICAL CHEMISTRY C

C: Surfaces, Interfaces, Porous Materials, and Catalysis

Simultaneous Optical and Electrical Characterization of GaN Nanowire Arrays by Means of Vis-IR Spectroscopic Ellipsometry

Antonio J. Santos, Bertrand Lacroix, Eduardo Blanco, Simon Hurand, Víctor J. Gómez, Fabien Paumier, Thierry Girardeau, Diana L. Huffaker, Rafael Garcia, and Francisco M. Morales

J. Phys. Chem. C, **Just Accepted Manuscript** • DOI: 10.1021/acs.jpcc.9b10556 • Publication Date (Web): 27 Dec 2019

is published by the American Chemical Society. 1155 Sixteenth Street N.W., Washington, DC 20036

Simultaneous Optical and Electrical Characterization of GaN Nanowire Arrays by Means of Vis-IR Spectroscopic Ellipsometry

Antonio J. Santos[1,2], Bertrand Lacroix[1,2], Eduardo Blanco[2,3], Simon Hurand[4], Víctor J. Gómez[5†], Fabien Paumier[4], Thierry Girardeau[4], Diana L. Huffaker[5,6], Rafael García[1,2] and Francisco M. Morales[1,2,]*

[1] Department of Materials Science and Metallurgic Engineering, and Inorganic Chemistry, Faculty of Sciences, University of Cádiz, Spain.

[2] IMEYMAT: Institute of Research on Electron Microscopy and Materials of the University of Cádiz, Spain.

[3] Department of Condensed Matter Physics, Faculty of Sciences, University of Cádiz, 11510 Puerto Real, Cádiz, Spain.

[4] Institut Pprime, UPR 3346 CNRS-Université de Poitiers-ENSMA, SP2MI, 86962 Futuroscope-Chasseneuil cedex, France.

[5] School of Engineering, Cardiff University, CF24 3AA, Cardiff, United Kingdom

[6] School of Physics and Astronomy, Cardiff University, CF24 3AA, Cardiff, United Kingdom

* Corresponding author: fmiguel.morales@uca.es

ABSTRACT

We report an original and straightforward method for both optical and electrical characterization of vertical GaN nanowire arrays epitaxially grown on silicon through visible-infrared spectroscopic ellipsometry methods. For the initial purpose of adding new inputs to the ellipsometry model, focused ion-beam tomography experiments were conducted to extract porosity/depth profiles of these systems. To reproduce the optical free-carrier behaviour in the infrared, the ellipsometric data acquired were fitted to an anisotropic Bruggeman model including Tauc-Lorentz and Drude oscillators, which

enabled the determination of carrier density and in-grain mobility. The nice agreement of these results with those obtained by combining Hall effect measurements, X-ray diffraction and transmission electron microscopy studies supported the validity of the proposed method, opening new horizons in the characterization of nanowire-based semiconducting layers.

INTRODUCTION

Gallium nitride (GaN) nanowire (NW) arrays grown by plasma-assisted molecular beam epitaxy (PAMBE) have recently attracted the attention of the scientific community due to their high crystalline quality and low defect density[1–4] and their unique electrical and optical properties[5–7]. By tuning the growth conditions, the size and arrangement of the nanowires, and thus the porosity, can be controlled so as to modulate the optical and electrical properties of the system[5,8–11]. Thanks to its high surface-to-volume ratio, tuneable refractive index and bandgap, high light extraction efficiency and quantum efficiency, GaN arrays have been erected as a promising material not only for the development of optoelectronic and optical devices such as field-effect transistors (FETs)[12,13], light-emitting diodes (LEDs)[6,14], laser diodes[15] and detectors[16], but also for photo-electrochemical water splitting[17,18] and energy storage[19] applications.

While the optical characterization of GaN nanowire and nanorod arrays through spectroscopic ellipsometry (SE)[9,10], polarized-goniometry[20] or reflectivity spectroscopy[11] is well reported in the literature, the characterization of electrical properties related to conductivity, like carrier concentration and mobility, presents some difficulties associated to the geometry of this kind of structures[4,21]. Up to now, the majority of the studies are focused on Hall effect and field effect measurements performed on single nanowires after fabricating multiple contacts[22–25]. However, given the challenges aforementioned, very few studies based on the electrical characterization of complete nanowire films have been reported at the time of the submission of this work[26–28]. Hence, the development of novel and alternative methodologies for the electrical characterization of nanowire layers, such as noncontact THz spectroscopic measurements[29], is crucial.

In this work, we report an alternative and straightforward way for both optical and electrical characterization of high-quality single crystalline GaN self-assembled NW films by means of visible-IR spectroscopic ellipsometry (SE), which is a cheap, fast, and non-destructive technique that can be used as a systematic characterization tool even for industrial processes. These porosity-controlled layers of GaN nanostructures were grown in a compact fashion by PAMBE. The porosity profiles along the layer thickness, which are not constant due to the presence of different nanostructures shapes from solid (SNW) to c-shape (CNW) and hollow (HNW) nanowires, were extracted through focused ion-beam (FIB) tomography reconstructions (slice and view). In order to reproduce the SE measurements, these porosity profiles were incorporated into an optical model through an effective-medium approximation in the framework of an anisotropic Bruggeman model, in which the optical constants of GaN are modelled by a combination of a Tauc-Lorentz oscillator and a Drude oscillator. This approach not only allows to determine porosity, thickness and optical constants of GaN NW films but also carrier densities and optical mobilities. The validity of the defined model is supported by combining Hall effect measurements, X-ray diffraction (XRD) and transmission electron microscopy (TEM) techniques including high-resolution (HRTEM) and energy-dispersive X-ray spectroscopy (EDX).

EXPERIMENTAL SECTION

Wurtzite GaN nanowire layers were grown on chemically cleaned p-type Si(111) or (100) substrates by PAMBE along the [0001] direction, and epitaxially aligned with the underlying Si substrate, following the same procedure as the one described in a previous study[10]. For 3D reconstructions, two different systems were used to acquire FIB-SEM tomography datasets: a Scios 2 DualBeam microscope from Thermo Scientific and a CrossBeam 350 microscope from ZEISS. Those datasets consist of stacks of SEM images recorded using backscattered electrons

and an acceleration voltage of 1.4 kV. The optical and electrical properties of each sample were evaluated by standard vis-IR spectroscopic ellipsometry at incident angles of 65°, 75° and 85°. These measurements were performed with a J. A. Woollam M2000XI (from 400 to 1700 nm) J. A. Woollam IR-VASE Mark II (from 1700 to 24000 nm), respectively. In order to confirm the veracity of the electrical properties obtained through vis-IR SE experiments, room temperature Hall Effect measurements were conducted using a Van der Pauw Ecopia AMP-55 Hall measurement system in the presence of a magnetic field. The crystallographic structure was investigated by X-ray diffraction (XRD) experiments which were performed using a Seifert XRD 3000 diffractometer fitted with a copper source and a 1 mm beam collimator. To obtain additional insights into the nanostructure, high-resolution transmission electron microscopy (TEM) experiments were conducted in a FEI Talos F200S analytical microscope operated at 200 kV and equipped with a Super-X energy-dispersive X-ray spectrometry (EDX) system that includes two silicon drift detectors. Local compositional analyses were performed by combining high-angle annular dark-field imaging (HAADF) and EDX acquisitions using the scanning (STEM) mode. Electron-transparent cross-sectional FIB lamellae were prepared for TEM observations by using the aforementioned FIB systems.

RESULTS AND DISCUSSION

With the additional purpose of examining the effect of substrate orientation on optical and electrical properties, the samples selected for this study were T2 and T2' (following the nomenclature of Ref. 10), i.e., the same growth conditions but different substrate orientations: Si(111) and Si(100), respectively.

These two samples are composed by a mixture of three different kind of NWs: SNWs filled and with hexagonal facets, HNWs, with solid bases which evolve into hollow structures when reaching a critical thickness, and CNWs, similar to HNWs but partially opened longitudinally. More in-depth studies of the structure and morphology of these three types of nanowires as well as the effect that growth conditions have on both the overall porosity and the optical properties of such systems can be found in Ref. 10. Due to the presence of this variety of nanostructures, the porosity profile along the Z direction turns uncertain and non-linear, hindering the optical characterization of these systems[30]. In order to overcome this difficulty, representative areas of T2 and T2' samples were explored with the aim of extracting their porosity profiles by performing FIB tomography experiments. In this regard, two different FIB systems (Thermo Scientific Scios 2 DualBeam and ZEISS CrossBeam 350) were employed to carry out 3D reconstructions and analyses of T2 and T2' volumes, respectively (see Supporting Information Section I for a detailed description of the experimental data acquisition, segmentation, 3D reconstruction and porosity profile extraction).

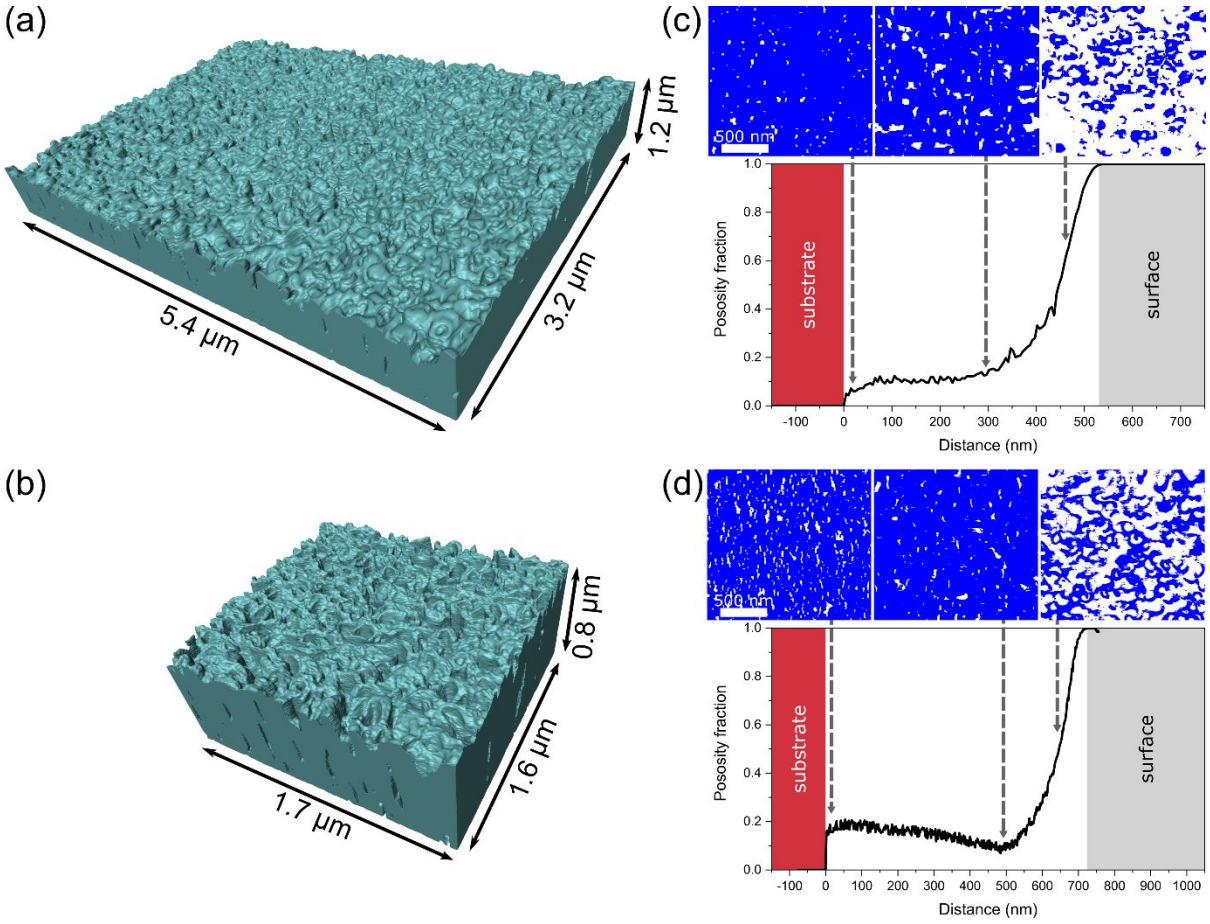

Figure 1. 3D reconstructions of the NW arrays in (a) T2 and (b) T2' samples through FIB tomography. Volume sizes are 5440 x 3222 x 1230 nm^3 and 1744 x 1602 x 834 nm^3, respectively. Porosity profiles of (c) T2 and (d) T2' samples extracted along the surface normal together with some planar views obtained by data segmentation at different depths (GaN material and voids are shown in blue and white colors, respectively). Note that these images were cut to show the same field of view in both samples, for comparison.

Figures 1(a) and (b) display volume visualizations of T2 and T2' samples respectively together with their porosity profiles along the surface normal (Fig. 1(c-d)). Note that the planar views obtained by data segmentation at depths close to the surface reveal the characteristic morphologies of GaN NWs (SNW, HNW and CNW). As a first approach, it can be appreciated a significant difference between the porosity profiles of both specimens. Whereas one of them (T2) experiences a first stage in which the porosity remains constant with the depth, followed by a progressive increase in porosity; the other (T2') firstly experiments a slight decrease in porosity up to reaching a critical thickness from which it increases sharply. Furthermore, there are also differences in the total thickness of both samples (around 550 nm and 750 nm for T2 and T2', respectively). In this way, the shapes of these two profiles only can be explained by considering that nanowires are composed by solid (filled) bases that evolve (or not) into hollow structures (HNW or CNW), justifying the initial step of constant porosity (first 300 nm of thickness) in sample T2. These results are consistent with the assumptions made in previous works[10]. On the other hand, the preliminary drop in porosity in sample T2' could be associated with the broadening of solid bases that occurs after attaining 100-150 nm thickness.

Once known the evolution of the porosity along the NW layer, vis-IR SE experiments were performed in areas close to 3D reconstructions with the purpose of conducting a full, accurate and comparable characterization of these systems. To do so, visible and infrared spectroscopic ellipsometry measurements were performed at incidence angles of 65º, 75º and 85º. Both spectra were acquired separately and then were spliced and treated with the WVASE software from J.A. Woollam. In a first stage of the study, the data acquired were fitted to an Anisotropic Bruggeman Effective Medium Approximation (ABEMA) model composed by a mixture of wurtzite GaN,

whose optical constants are modelled by the ones obtained for high-quality single-crystalline α-GaN layers[31], and void. A 2-nm-thick layer of silicon nitride (Si_3N_4) located between the Si substrate and the nanowire layer was also included in the optical model. With the aim of reflecting the columnar geometry of the film with NWs growing perpendicular to the substrate, the depolarization factor in the extraordinary (out-of-plane) direction (q_z) was fixed to 0, whereas the ordinary or in-plane ones (q_x and q_y) were fixed at 1/2 (uniaxial anisotropy)[32,33]. Moreover, the porosity profiles extracted by FIB tomography 3D reconstructions were incorporated into the model in order to reproduce the variation in the refractive index (n) along the Z direction (as a function based graded-index layer). On the other side, the anisotropy associated to the wurtzite GaN structure was considered negligible compared to the anisotropy associated to the columnar structure. Indeed, wurtzite GaN has a uniaxial structure, and its intrinsic birefringence, which is the difference $\Delta n = n_z - n_{x,y}$ between extraordinary optical index n_z and ordinary one $n_{x,y}$ is of the order of 0.02 (in absolute terms) in the visible range according to Ref. 31 (see Supporting Information Figure S8). On the other hand, by modelling GaN as an isotropic material and implementing it into the ABEMA model above mentioned, the birefringence in the visible range is around 0.1 in the visible range as one can see on Figure 2(c) and 2(d), that is, 5 times higher than the intrinsic birefringence of wurtzite GaN. We may therefore neglect the intrinsic uniaxial structure of GaN, and conclude that the observed anisotropy is mainly due to the elongated shape of the NWs.

Despite this model provides a fine agreement to the experimental data in the visible range, it fails to reproduce the absorption in the IR range, as can be seen on Figure 2(a) and 2(b). Indeed, the presence of a weak but non-negligible level of doping in the GaN results in free carrier absorption in the IR range. In order to model correctly this absorption, we replace the tabulated optical

constants from Ref. 31 for wurtzite GaN by a combination of two oscillators: (i) a Tauc-Lorentz Oscillator (TLO) modelling the direct band gap (E_g) absorption of GaN[34]; and (ii) a Drude Oscillator (DO) modelling the free-carrier behaviour in the IR range[35] (a scheme of the optical model is presented in Supporting Information Figure S2). From 1.5 to 3 eV, that is, in the visible range, the parameters of the TLO were adjusted onto the values of the dielectric constants for wurtzite GaN from the Ref. 31. The advantage of using a Tauc-Lorentz oscillator over, e.g., a simple Lorentz oscillator is to impose a more realistic value of zero for ε_2 below the gap. Also, a TLO permits the combination with another oscillator, here a Drude oscillator, unlike, e.g., a simple Cauchy model. In this way, a DO was incorporated to represent free-carrier absorption by fitting the ellipsometry data in the lower energy region, considering an effective mass (m^*) of 0.20 for wurtzite GaN[36] , while the free carrier density $N_{e(opt)}$ and optical mobility μ_{opt} are the parameters to be fitted. Indeed, the Drude model is appropriate to characterize samples with carrier concentrations down to 10^{18} cm^{-3} when infrared spectroscopic ellipsometry is used[37].

The fittings obtained for T2 and T2' samples after incorporating TLO and DO models are shown in Fig. 2(a) and (b) respectively, together with the fitting obtained by using either a TLO alone (TLO) or the data from Ref. 31 (Adachi) for GaN. As one can see, a TLO alone or Adachi data provide a quite good description of the measured Ψ and Δ SE values in the visible range. However, while approaching the IR range, a shift in energy between the modelled and measured oscillations of Ψ and Δ is noticeable. Moreover, they predict oscillations below 0.4 eV that are not observed. The addition of a Drude oscillator to the model resolves these issues: the modelled oscillations of Ψ and Δ remain in phase with the measured ones even in the IR range, and their cut-off at 0.4 eV is correctly predicted. We emphasize here that this cut-off provides a very robust criterion to fit the carrier density: the Mean Square Error (MSE) increases by 10% when a relative change of 10%

of $N_{e(opt)}$ is applied to the model (see Supporting Information Figure S6). With this criterion, the relative uncertainty on the fitted value of $N_{e(opt)}$ is ± 10%, for values of $N_{e(opt)}$ as low as 1 x 10^{18} e/cm^3. That is, ± 0.1 x 10^{20} e/cm^3 for a fitted value of $N_{e(opt)}$ = 1.3 x 10^{20} e/cm^3 for sample T2.

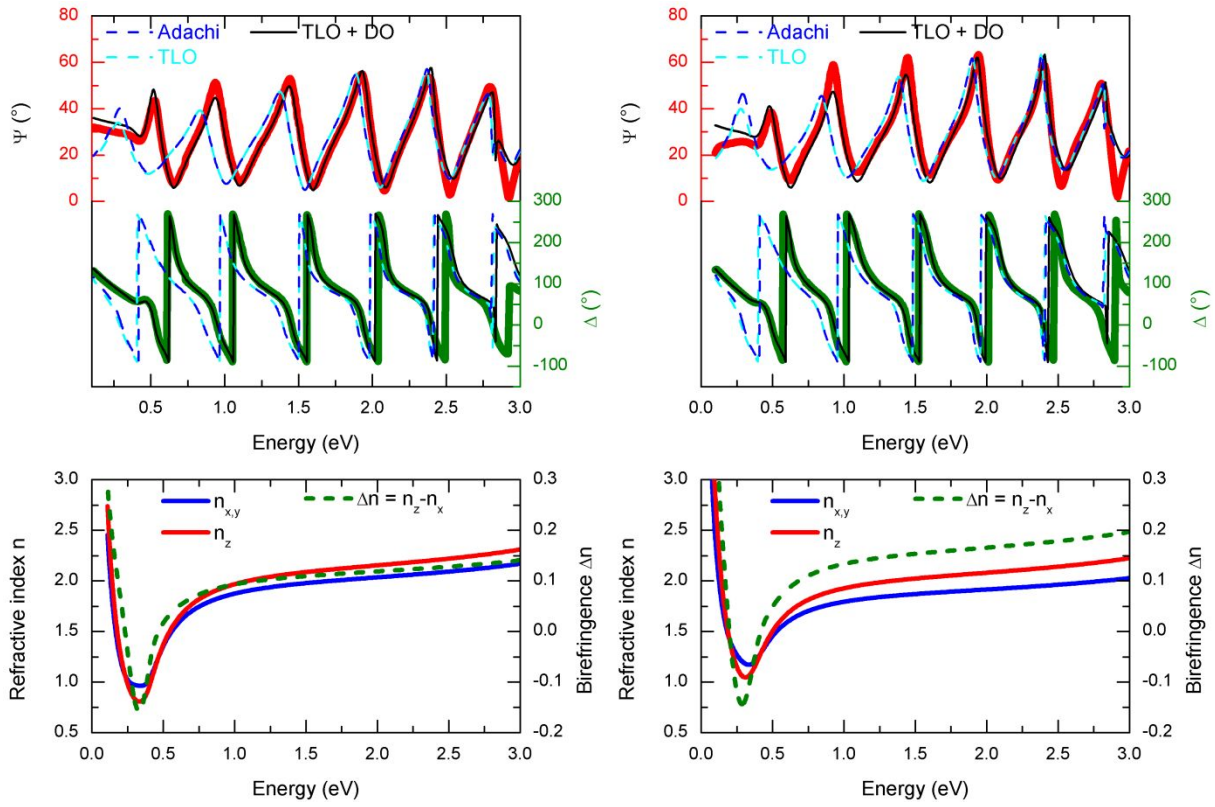

Figure 2. Measured spectroscopic ellipsometry angles Ψ (red) and Δ (green) for (a) T2 and (b) T2' samples at an incident angle of 65°. Thick solid lines represent the experimental measurements. Thin solid black lines represent the best-fit achieved using the SE model (ABEMA including TLO + DO). For comparison, dashed lines represent the best-fit obtained with an ABEMA model with only a TLO (light blue) or using Adachi et al. (Ref. 31) data (dark blue) for GaN. In-plane (blue solid lines) and out-of-plane (red solid lines) refractive indices and

birefringence (dashed green lines) of (c) T2 and (d) T2' samples obtained from simulations using the SE model.

The evolutions of the in-plane and out-of-plane refractive indices along with the birefringence of T2 and T2' NW layers, obtained from the enhanced ellipsometry model over the vis-IR range, are displayed in Fig. 2(c) and (d), respectively. As expected, the refractive indices of both samples in the visible spectrum are smaller than that of bulk GaN due to the presence of voids. Nevertheless, both layers start to experience a metallic behaviour at energies around 0.4 eV which corresponds to the onsets of free-carrier absorption, leading to an increase in refractive indices. Also note that, from visible to near infrared, the refractive indices in the Z direction are greater than that corresponding to the in-plane one. Likewise, the values of birefringence obtained in this spectral range let us evidence that the optical anisotropy in T2' is stronger than in T2.

Additionally, the DO parameters ($N_{e(opt)}$ and μ_{opt}) provided by the SE model are $N_{e(opt)}$ (T2) = (1.3 ± 0.1) x 10^{20} e^-/cm^3 and μ_{opt} (T2) = 45 ± 5 $cm^2/V{\cdot}s$; $N_{e(opt)}$ (T2') = (1.1 ± 0.1) x 10^{20} e^-/cm^3 and μ_{opt} (T2') = 34 ± 5 $cm^2/V{\cdot}s$. Note that the doping level of both samples is surprisingly high, taking into account that they were not intentionally doped. Regarding the optical mobility, the values extracted from the SE model are in good agreement with the electrical mobility obtained in the literature by four-point measurement for single GaN NWs[4,38]. Besides, these results are also consistent with the values of mobility obtained from the Hilsum equation[39] adapted for the case of GaN NWs[40], that is, 32.2 $cm^2/V{\cdot}s$ for T2 and 33.2 $cm^2/V{\cdot}s$ for T2' considering the doping level predicted by the SE model. This is because the optical measurements performed supply intra-granular information, which is equivalent to the mean of a set of measurements carried out on different single NWs.

In order to confirm the values of carrier density and mobility predicted by SE as well as to validate the defined model, room temperature Hall Effect measurements were conducted. For this purpose, four contacts were placed at the corners of squared-shaped samples which were cut in such way that the same areas as in previous experiments were studied.

	Sample T2	Sample T2'
Hall voltage, V_H (V)	$(-4.4 \pm 0.2)\cdot 10^{-6}$	$(-4.4 \pm 0.9)\cdot 10^{-6}$
Sheet Resistance, R_s (Ω)	111.5 ± 0.1	1881.2 ± 6.0
Hall carrier density, $N_{e(Hall)}$ (e-/cm^3)	$(1.6 \pm 0.1)\cdot 10^{20}$	$(1.2 \pm 0.3)\cdot 10^{20}$
Hall mobility, μ_{Hall} (cm^2/V·s)	6.8 ± 0.3	0.4 ± 0.1
Optical carrier density, $N_{e(opt)}$ (e-/cm^3)	$(1.3 \pm 0.1)\cdot 10^{20}$	$(1.1 \pm 0.1)\cdot 10^{20}$
Optical mobility, μ_{opt} (cm^2/V·s)	45 ± 5	34 ± 5

Table 1. Summary of the electrical characterization of T2 and T2' samples through Hall Effect measurements and vis-IR SE. Hall effect experiments were conducted by supplying a current of 100 μA and inducing a magnetic field of 0.58 T. The thicknesses considered for these calculations were the obtained from 3D reconstructions (Fig. 1).

An overview of the results obtained from the Hall effect measurements for T2 and T2' samples can be found in Table.1. The negative sign of the Hall voltage indicates that the majority of the carriers were electrons for both samples (n-type semiconductor). Moreover, the values of carrier densities measured are in accordance with those predicted by SE, which confirms the high n-doping level. However, great differences between the electrical behaviour of T2 and T2' samples are observed. As can be seen, sample T2' exhibits a greater opposition to the flow of electric current than T2 (just over one order of magnitude). It should be also noted that the mobility measured by Hall effect, in addition to be surprisingly low, does not correspond with the one predicted by the SE model. The latter is expectable since SE provides information related to the free-carrier mobility within grains (μ_{opt}) while Hall effect give us information about the total mobility of the layer (μ_{Hall}), including the effects of grain boundaries as well as the porosity of the structure. Conversely, $N_{e(Hall)}$ values are not affected by the porosity[41], so it is relevant to compare them directly with those resulting from SE ($N_{e(opt)}$). Thus, μ_{Hall} values suggest that the mobility in GaN NW arrays is dominated by inter-grain barriers.

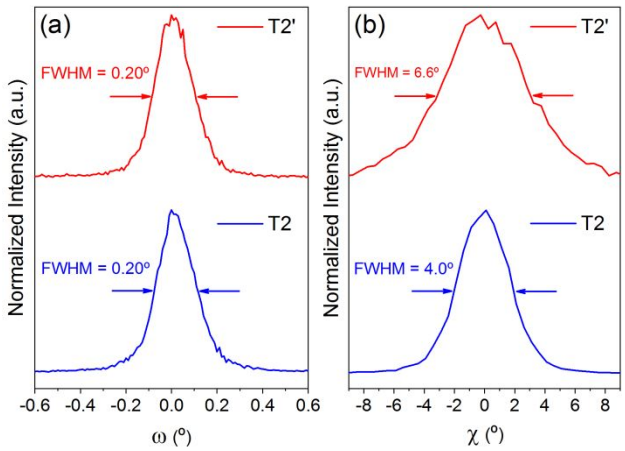

Figure 3. XRD rocking curves: (a) ω-scans and (b) χ-scans of the GaN 0002 reflection for T2 (blue lines) and T2' (red lines) samples.

This assumption is also supported by the shape analyses of XRD rocking curves (ω and χ-scans) of 0002 GaN diffraction peaks. As can be appreciated in Fig. 3(a), the full width at half maximum (FWHM) values of the ω-scans are rather small for T2 and T2' samples (0.20º in both cases) which not only indicates the good crystal quality of nanowires (low density of dislocations) but also a good epitaxial alignment between the GaN nanostructure and the single-crystalline Si substrate (the out-of-plane epitaxial relationship is GaN(0001)||Si(111) for T2 and GaN(0001)||Si(001) for T2'). In addition, χ-scans (Fig. 3(b)) reveal that the slight misorientation of the (0002) planes along the growth direction (tilt) is more significant in T2' than in T2.

Once come to this point, it is time to account for the unintentional high doping concentration of the GaN NW layers. With the aim of elucidating the origin of the doping, EDX chemical analyses were carried out in both samples. The Thermo Scientific Velox ™ user interface was used for data acquisition and processing. Quantification of the EDX data was performed using the standardless method. In order to minimize errors during this step, intensities of the different peaks were extracted with a great care after background subtraction with a multi-polynomial approach. Since this approach can lead to inaccuracy in the quantitative composition determination, especially for low *Z* elements like O and N, qualitative analyses were conducted. STEM high-angle annular dark field imaging (HAADF) and EDX elemental maps (see Fig. 4(a-b)) reveal a remarkable presence of oxygen distributed throughout both films. Note that the oxygen signal becomes greater on the

edges of the nanowires, where projections only bring contributions of the surrounding material, suggesting that oxygen is mainly accumulated at NW surfaces (see elemental profiles obtained for both samples in Figure 5(a-b)). Likewise, EDX normalized spectra (Fig. 4(c)) of both samples reveal that the amount of oxygen in T2' is larger than the one detected in T2. In this context, it is well known that high concentrations of oxygen in GaN can cause high levels of electron concentration[42–45]. Therefore, in consideration of these results, it could be assumed that the observed GaN NWs doping is linked to oxygen impurities.

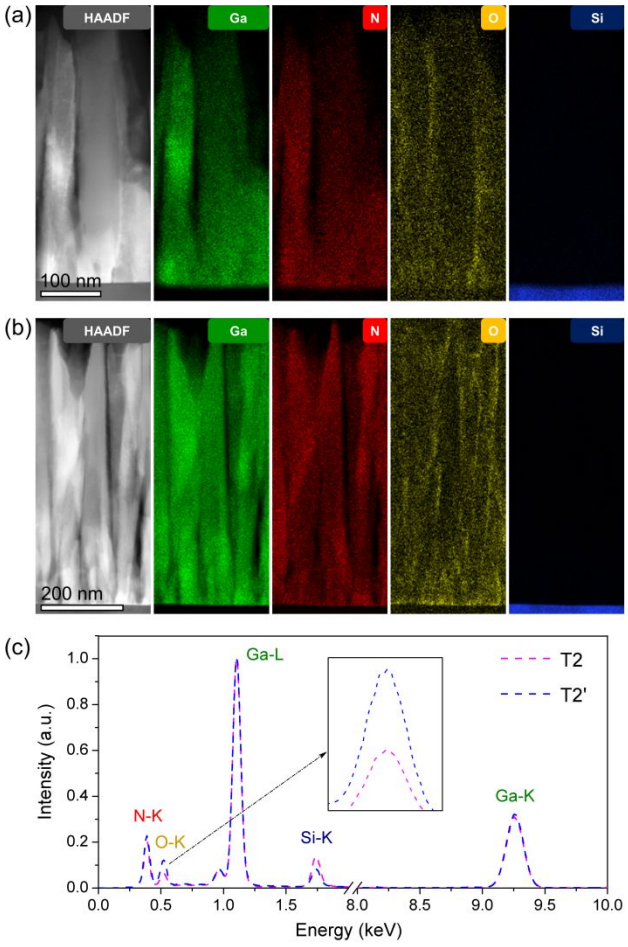

Figure 4. STEM-HAADF and EDX elemental maps of (a) T2 and (b) T2' samples obtained for Ga, N, O and Si atoms. (c) EDX spectra, normalized at Ga-L_α peak (1098 eV), for T2

(magenta dashed line) and T2' (blue dashed line) samples. The inset corresponds to the feature of the O-K_α peak (525 eV).

By contrast, the explanation for the low total mobility of such GaN nanostructures is more complex. In addition to the effect of porosity, which acts by reducing the volume in which the current flows[46], two additional reasons could contribute to this phenomenon: (i) surface state trapping; and (ii) the formation of native oxide on the surface. Generally, electrical properties of nanowire-structured semiconductors are sensitive to the status of their surfaces. One of the main problems of nanostructured systems is the decrease in the carrier mobility due to the scattering from the surface states. Furthermore, this effect becomes even more significant for the case of NWs because of their high surface-to-volume ratio, which leads to free carriers within the wire being trapped at surface traps[16,47]. Nonetheless, this phenomenon would only affect the mobility inside nanowires which was proved not to be the responsible for the low total mobility of the studied systems.

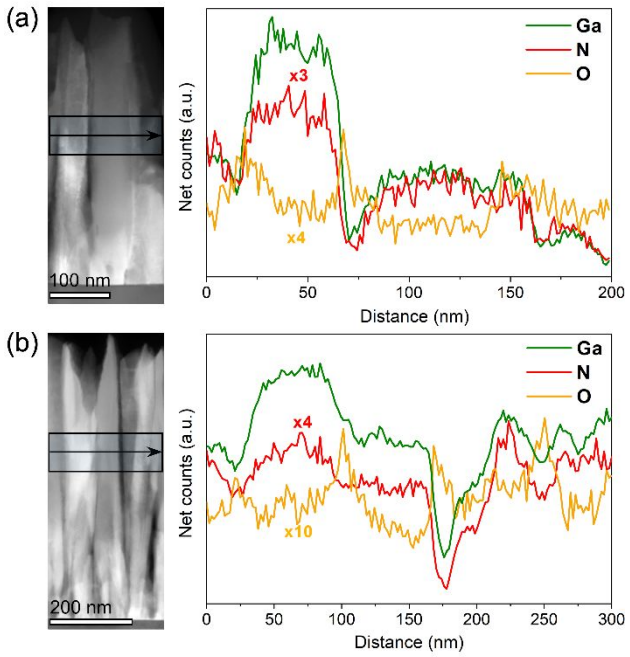

Figure 5. STEM-HAADF and Ga, N and O EDX elemental profiles for (a) T2 and (b) T2' samples. Note that such profiles were integrated across the NWs following the direction indicated by the arrows.

Another consequence of the great surface-to-volume ratio is the formation of amorphous layers of native oxide surrounding the nanowires when they are exposed to air. This issue has been previously reported by other authors[21,48] resulting in a detrimental effect on electrical properties since this oxide shell acts as a barrier for the motion of electrons among nanowires. According to similar studies[49,50], this fact might also provide an explanation for the high levels of electron concentration in these GaN nanostructures: part of the oxygen atoms could diffuse from the oxide layer into the GaN nanowire at room temperature, originating oxygen impurities. HRTEM micrographs and fast Fourier transform (FFT) diffractions of isolated wurtzite GaN nanowires of T2 (Fig. 6(a)) and T2' (Fig. 6(b)) samples evidence this formation of amorphous layers of native

oxide on the surface. Note that the amount of oxide generated on the surface of the nanowire belonging to T2' is considerably larger than that observed in the NW of T2. The latter, in addition to supporting the results obtained through EDX analyses, could be associated to a major susceptibility to oxidation of T2' compared to T2 sample, leading to a minor mobility of the T2' sample as Hall effect measurements revealed. Thus, we propose that both the native oxide layer formed on cylinder-like surfaces and porosity are the limiting factors on the global mobility of GaN nanowire arrays films.

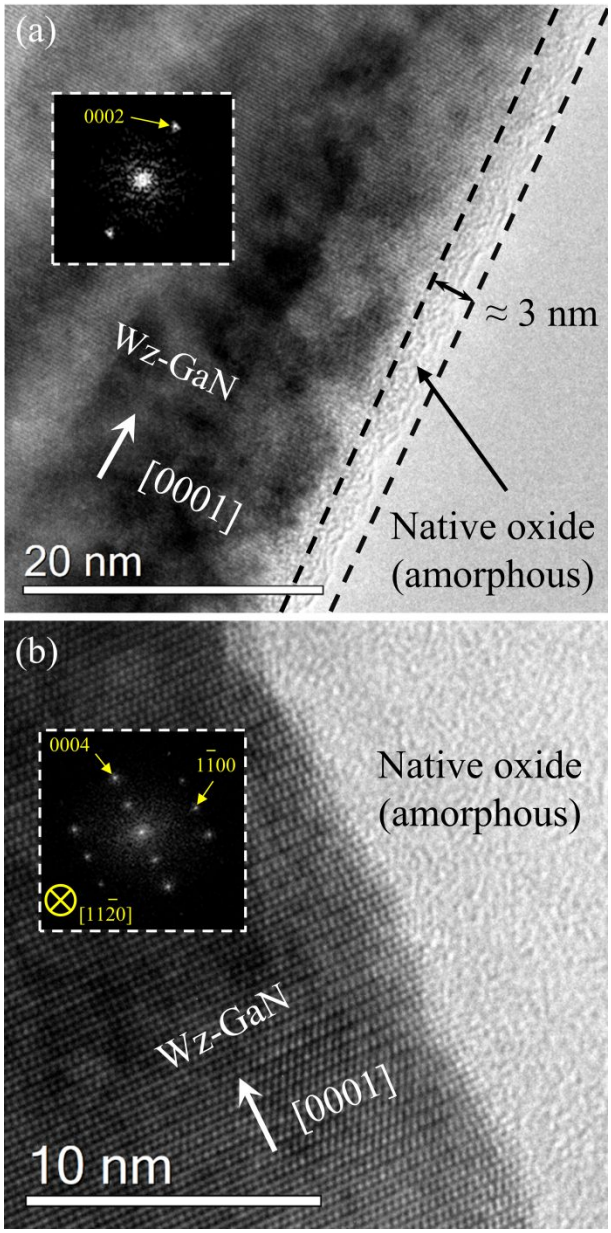

Figure 6. High-resolution TEM micrographs and corresponding FFT diffractions of single nanowires of (a) T2 and (b) T2' samples. Note that these TEM observations were conducted on two FIB lamellae prepared by using the same SEM-FIB systems as for FIB tomography experiments.

After reaching these conclusions, it is clear that surface-to-volume ratio plays a vital role in both optical and electrical properties of GaN NW arrays. The insertion of porosity allows to cut down the effective refractive index of the layer. However, increasing the porosity implies greater surface-to-volume ratios, which has been proved to have a detrimental effect on the electron mobility because the formation of native oxide shells within the semiconducting layers is favoured when the surface exposed to air is greater[51]. Hence, by tuning the growth conditions, the porosity of the nanostructures can be controlled, making these systems more appropriate for optical or electrical applications.

CONCLUSIONS

In summary, optical and electrical properties of GaN nanowire arrays grown on Si (111) and Si (100) by PAMBE were simultaneously explored by means of an innovative methodology based on vis-IR spectroscopic ellipsometry. For a better description of these nanostructures, porosity profiles extracted by FIB tomography reconstructions were implemented into an ABEMA model where the optical constants of GaN were modelled by a multioscillator approach (TLO and DO) which enabled us to determine the carrier density and intra-grain mobility of such nanostructures. These results evidenced electron concentrations of about 10^{20} cm^{-3} and optical mobilities comparable to the one reported for individual GaN nanowires (30-50 $cm^2/V \cdot s$). Hall effect measurements, XRD and transmission electron microscopy (STEM-EDX and HRTEM) studies not only provided a confirmation of the results predicted by the SE model but also let us elucidate that the oxygen impurity was the responsible for the high doping level and that the total mobility

of such GaN arrays was mainly limited by the combined effect of porosity and surface oxidation of individual nanowires.

ASSOCIATED CONTENT

Supporting Information.

Three-dimensional FIB-SEM tomography reconstructions (experimental data acquisition; data processing; alignment, rotation, cropping and denoising; segmentation and porosity quantification), optical modeling (optical model; fitting procedure; relevance of the Drude Oscillator; lowest detectable carrier concentration; uncertainty of the fit parameters; intrinsic anisotropy of GaN; plasmonic effects) and additional references.

AUTHOR INFORMATION

Corresponding Author

* Email: fmiguel.morales@uca.es

Present Addresses

† Present address: Solid State Physics, Lund University, Box 118, S-221 00 Lund, Sweden.

Author Contributions

The manuscript was written through contributions of all authors. All authors have given approval to the final version of the manuscript.

ACKNOWLEDGMENTS

The authors would like to express their gratitude to Ellen Backen, applications scientist from Thermo Fisher Scientific, for the images registered at the Scios 2 HiVac system at Nanoport (Eindhoven). We would also like to acknowledge ZEISS corporations for technical assistance as well as the loaning of the CrossBeam 350 system and the data acquisition. A. J. Santos would like to thank the IMEYMAT Institute and the Spanish Ministerio de Educación y Cultura for the concessions of grants (ICARO-173873 and FPU16-04386). The “Talent Attraction Program” of the University of Cádiz is acknowledged by supporting B. Lacroix contract code E-11-2017-0117214. University of

Cádiz and IMEYMAT are also agreed by financing the mutual facilities available at the UCA R&D Central Services (SC-ICYT), the UCA project reference “PUENTE PR2018-040”, and the IMEYMAT project reference “AGREGADOR 2018-1”. The authors would like to acknowledge the financial support provided by Sêr Cymru National Research Network in Advanced Engineering and Materials. This work was also supported by the IMATOP project funded by “Nouvelle Aquitaine” Region and by the European Structural and Investment Funds (ERDF reference P-2016-BAFE-209).

REFERENCES

(1) Sobanska, M. Comprehensive Analysis of the Self-Assembled Formation of GaN Nanowires on Amorphous Al_xO_y: In Situ Quadrupole Mass Spectrometry Studies. *Nanotechnology* **2019**, *30* (15), 154002.

(2) Bolshakov, A. D.; Mozharov, A. M.; Sapunov, G. A.; Shtrom, I. V.; Sibirev, N. V.; Fedorov, V. V.; Ubyivovk, E. V.; Tchernycheva, M.; Cirlin, G. E.; Mukhin, I. S. Dopant-Stimulated Growth of GaN Nanotube-like Nanostructures on Si(111) by

Molecular Beam Epitaxy. *Beilstein J. Nanotechnol.* **2018**, *9* (1), 146–154.

(3) Schlager, J. B.; Sanford, N. A.; Bertness, K. A.; Barker, J. M.; Roshko, A.; Blanchard, P. T. Polarization-Resolved Photoluminescence Study of Individual GaN Nanowires Grown by Catalyst-Free Molecular Beam Epitaxy. *Appl. Phys. Lett.* **2006**, *88* (21), 1–4.

(4) Mansfield, L. M.; Bertness, K. A.; Blanchard, P. T.; Harvey, T. E.; Sanders, A. W.; Sanford, N. A. GaN Nanowire Carrier Concentration Calculated from Light and Dark Resistance Measurements. *J. Electron. Mater.* **2009**, *38* (4), 495–504.

(5) Pauzauskie, P. J.; Yang, P. Nanowire Photonics. *Mater. Today* **2006**, *9* (10), 36–45.

(6) Chen, C. Y.; Zhu, G.; Hu, Y.; Yu, J. W.; Song, J.; Cheng, K. Y.; Peng, L. H.; Chou, L. J.; Wang, Z. L. Gallium Nitride Nanowire Based Nanogenerators and Light-Emitting Diodes. *ACS Nano* **2012**, *6* (6), 5687–5692.

(7) Barrigón, E.; Heurlin, M.; Bi, Z.; Monemar, B.; Samuelson, L. Synthesis and

Applications of III–V Nanowires. *Chem. Rev.* **2019**, *119* (15), 9170–9220.

(8) Park, Y. S.; Lee, G.; Holmes, M. J.; Chan, C. C. S.; Reid, B. P. L.; Alexander-Webber, J. A.; Nicholas, R. J.; Taylor, R. A.; Kim, K. S.; Han, S. W.; et al. Surface-Effect-Induced Optical Bandgap Shrinkage in GaN Nanotubes. *Nano Lett.* **2015**, *15* (7), 4472–4476.

(9) Lee, J. H.; Lee, B.; Kang, J. H.; Lee, J. K.; Ryu, S. W. Optical Characterization of Nanoporous GaN by Spectroscopic Ellipsometry. *Thin Solid Films* **2012**, *525*, 84–87.

(10) Gómez, V. J.; Santos, A. J.; Blanco, E.; Lacroix, B.; García, R.; Huffaker, D. L.; Morales, F. M. Porosity Control for Plasma-Assisted Molecular Beam Epitaxy of GaN Nanowires. *Cryst. Growth Des.* **2019**, *19* (4), 2461–2469.

(11) Chen, H.-Y.; Lin, H.-W.; Wu, C.-Y.; Chen, W.-C.; Chen, J.-S.; Gwo, S. Gallium Nitride Nanorod Arrays as Low-Refractive-Index Transparent Media in the Entire Visible Spectral Region. *Opt. Express* **2008**, *16* (11), 8106.

(12) Cha, H. Y.; Wu, H.; Chandrashekhar, M.; Choi, Y. C.; Chae, S.; Koley, G.; Spencer, M. G. Fabrication and Characterization of Pre-Aligned Gallium Nitride Nanowire Field-Effect Transistors. *Nanotechnology* **2006**, *17* (5), 1264–1271.

(13) Wu, H.; Cha, H. Y.; Chandrashekhar, M.; Spencer, M. G.; Koley, G. High-Yield GaN Nanowire Synthesis and Field-Effect Transistor Fabrication. *J. Electron. Mater.* **2006**, *35* (4), 670–674.

(14) Yeh, P. C.; Hwa, M. C.; Yu, J. W.; Wu, H. M.; Tsai, H. L.; Lai, C. M.; Huang, J. J.; Yang, J. R.; Peng, L. H. Photon-Assisted Tunneling in GaN Nanowire White Light Emitting Diodes. *Phys. Status Solidi Curr. Top. Solid State Phys.* **2009**, *6* (SUPPL. 2), 538–540.

(15) Gradečak, S.; Qian, F.; Li, Y.; Park, H. G.; Lieber, C. M. GaN Nanowire Lasers with Low Lasing Thresholds. *Appl. Phys. Lett.* **2005**, *87* (17), 1–3.

(16) Sun, J.; Han, M.; Gu, Y.; Yang, Z. xing; Zeng, H. Recent Advances in Group III–V Nanowire Infrared Detectors. *Adv. Opt. Mater.* **2018**, *6* (18), 1–17.

(17) Ryu, S. W.; Zhang, Y.; Leung, B.; Yerino, C.; Han, J. Improved Photoelectrochemical Water Splitting Efficiency of Nanoporous GaN Photoanode. *Semicond. Sci. Technol.* **2012**, *27* (1), 015014.

(18) Park, J.; Mandal, A.; Kang, S.; Chatterjee, U.; Kim, J. S. Hydrogen Generation Using Non- Polar Coaxial InGaN/GaN Multiple Quantum Well Structure Formed on Hollow n-GaN Nanowires. *Sci. Rep.* **2016**, *6*, 31996.

(19) Zhang, L.; Wang, S.; Shao, Y.; Wu, Y.; Sun, C.; Huo, Q.; Zhang, B.; Hu, H.; Hao, X. One-Step Fabrication of Porous GaN Crystal Membrane and Its Application in Energy Storage. *Sci. Rep.* **2017**, *7*, 1–9.

(20) Henneghien, A.-L.; Tourbot, G.; Daudin, B.; Lartigue, O.; Désières, Y.; Gérard, J.-M. Optical Anisotropy and Light Extraction Efficiency of MBE Grown GaN Nanowires Epilayers. *Opt. Express* **2011**, *19* (2), 527.

(21) Gurwitz, R.; Shalish, I. Method for Electrical Characterization of Nanowires. *Nanotechnology* **2011**, *22* (43), 435705.

(22) Motayed, A.; Vaudin, M.; Davydov, A. V.; Melngailis, J.; He, M.; Mohammad, S. N. Diameter Dependent Transport Properties of Gallium Nitride Nanowire Field Effect Transistors. *Appl. Phys. Lett.* **2007**, *90* (4), 15–18.

(23) Storm, K.; Halvardsson, F.; Heurlin, M.; Lindgren, D.; Gustafsson, A.; Wu, P. M.; Monemar, B.; Samuelson, L. Spatially Resolved Hall Effect Measurement in a Single Semiconductor Nanowire. *Nat. Nanotechnol.* **2012**, *7* (11), 718–722.

(24) Huang, Y.; Duan, X.; Cui, Y.; Lieber, C. M. Gallium Nitride Nanowire Nanodevices. *Nano Lett.* **2002**, *2* (2), 101–104.

(25) Hultin, O.; Otnes, G.; Borgström, M. T.; Björk, M.; Samuelson, L.; Storm, K. Comparing Hall Effect and Field Effect Measurements on the Same Single Nanowire. *Nano Lett.* **2016**, *16* (1), 205–211.

(26) Roddaro, S.; Nilsson, K.; Astromskas, G.; Samuelson, L.; Wernersson, L. E.; Karlström, O.; Wacker, A. InAs Nanowire Metal-Oxide-Semiconductor Capacitors. *Appl. Phys. Lett.* **2008**, *92* (25), 253509.

(27) Chen, Z. H.; Tang, Y. B.; Liu, Y.; Yuan, G. D.; Zhang, W. F.; Zapien, J. A.; Bello, I.; Zhang, W. J.; Lee, C. S.; Lee, S. T. ZnO Nanowire Arrays Grown on Al:ZnO Buffer Layers and Their Enhanced Electron Field Emission. *J. Appl. Phys.* **2009**, *106* (6), 0–6.

(28) Wen, X.; Wu, W.; Ding, Y.; Wang, Z. L. Seedless Synthesis of Patterned ZnO Nanowire Arrays on Metal Thin Films (Au, Ag, Cu, Sn) and Their Application for Flexible Electromechanical Sensing. *J. Mater. Chem.* **2012**, *22* (19), 9469–9476.

(29) Parkinson, P.; Dodson, C.; Joyce, H. J.; Bertness, K. A.; Sanford, N. A.; Herz, L. M.; Johnston, M. B. Noncontact Measurement of Charge Carrier Lifetime and Mobility in GaN Nanowires. *Nano Lett.* **2012**, *12* (9), 4600–4604.

(30) Zangooie, S.; Woollam, J. A. Ellipsometric Characterization of Thin Porous GaAs Layers. *J. Mater. Sci. Lett.* **2000**, 2171–2173.

(31) Adachi, S. *Optical Constants of Crystalline and Amorphous Semiconductors*; Springer Science: Boston, MA, 1999.

(32) Jones, S. B.; Friedman, S. P. Particle Shape Effects on the Effective Permittivity of Anisotropic or Isotropic Media Consisting of Aligned or Randomly Oriented Ellipsoidal Particles. *Water Resour. Res.* **2000**, *36* (10), 2821–2833.

(33) Kaminska, K.; Amassian, A.; Martinu, L.; Robbie, K. Growth of Vacuum Evaporated Ultraporous Silicon Studied with Spectroscopic Ellipsometry and Scanning Electron Microscopy. *J. Appl. Phys.* **2005**, *97* (1), 013511.

(34) Jellison, G. E.; Modine, F. A. Parameterization of the Optical Functions of Amorphous Materials in the Interband Region. *Appl. Phys. Lett.* **1996**, *69* (3), 371–373.

(35) Fujiwara, H.; Kondo, M. Effects of Carrier Concentration on the Dielectric Function of ZnO:Ga and In_2O_3:Sn Studied by Spectroscopic Ellipsometry: Analysis of Free-Carrier and Band-Edge Absorption. *Phys. Rev. B - Condens. Matter Mater. Phys.* **2005**, *71* (7), 1–10.

(36) Drechsler, M.; Hofmann, D. M.; Meyer, B. K.; Detchprohm, T.; Amano, H.; Akasaki,

I. Determination of the Conduction Band Electron Effective Mass in Hexagonal Gan. *Jpn. J. Appl. Phys.* **1995**, *34* (9), L1177–L1179.

(37) Fujiwara, H. *Spectroscopic Ellipsometry: Principles and Applications*; John Wiley & Sons Inc: Chichester, 2007.

(38) Chang, C. Y.; Chi, G. C.; Wang, W. M.; Chen, L. I. C.; Chen, K. H.; Ren, F.; Pearton, S. J. Electrical Transport Properties of Single GaN and InN Nanowires. *J. Electron. Mater.* **2006**, *35* (4), 738–743.

(39) Hilsum, C. Simple Empirical Relationship between Mobility and Carrier Concentration. *Electron. Lett.* **1974**, *10* (13), 259–260.

(40) Benner, O.; Blumberg, C.; Arzi, K.; Poloczek, A.; Prost, W.; Tegude, F. J. Electrical Characterization and Transport Model of N-Gallium Nitride Nanowires. *Appl. Phys. Lett.* **2015**, *107* (8), 1–5.

(41) Orton, J. W.; Powell, M. J. The Hall Effect in Polycrystalline and Powdered Semiconductors. *Reports Prog. Phys.* **1980**, *43* (11), 1263–1307.

(42) Xie, Z.; Sui, Y.; Buckeridge, J.; Sokol, A. A.; Keal, T. W.; Walsh, A. Prediction of Multiband Luminescence Due to the Gallium Vacancy-Oxygen Defect Complex in GaN. *Appl. Phys. Lett.* **2018**, *112* (26), 1–16.

(43) Seifert, W.; Franzheld, R.; Butter, E.; Sobotta, H.; Riede, V. On the Origin of Free Carriers in High-conducting N-GaN. *Cryst. Res. Technol.* **1983**, *18* (3), 383–390.

(44) Kumar, M.; Poulose, A. C.; Nakajima, Y.; Sakthikumar, D.; Kumar, V.; Singh, R. Anomalous Emission from Oxygen Incorporated GaN Nanowires. *Phys. E Low-Dimensional Syst. Nanostructures* **2018**, *104*, 187–191.

(45) Slack, G. A.; Schowalter, L. J.; Morelli, D.; Freitas, J. A. Some Effects of Oxygen Impurities on AlN and GaN. *J. Cryst. Growth* **2002**, *246* (3–4), 287–298.

(46) Feenstra, R. M.; Wood, C. E. C. *Porous Silicon Carbide and Gallium Nitride*; John Wiley & Sons Inc: Chichester, 2008.

(47) Shalish, I.; Temkin, H.; Narayanamurti, V. Size-Dependent Surface Luminescence in ZnO Nanowires. *Phys. Rev. B - Condens. Matter Mater. Phys.* **2004**, *69* (24),

1–4.

(48) Watkins, N. J.; Wicks, G. W.; Gao, Y. Oxidation Study of GaN Using X-Ray Photoemission Spectroscopy. *Appl. Phys. Lett.* **1999**, *75* (17), 2602–2604.

(49) Pearton, S. J.; Cho, H.; LaRoche, J. R.; Ren, F.; Wilson, R. G.; Lee, J. W. Oxygen Diffusion into SiO_2-Capped GaN during Annealing. *Appl. Phys. Lett.* **1999**, *75* (19), 2939–2941.

(50) Jakiela, R.; Dumiszewska, E.; Caban, P.; Stonert, A.; Turos, A.; Barcz, A. Oxygen Diffusion into GaN from Oxygen Implanted GaN or Al_2O_3. *Phys. Status Solidi Curr. Top. Solid State Phys.* **2011**, *8* (5), 1513–1515.

(51) Santos, A. J.; Lacroix, B.; Maudet, F.; Corvisier, A.; Paumier, F.; Dupeyrat, C.; Girardeau, T.; García, R.; Morales, F. M. Surface Oxidation of Amorphous Si and Ge Slanted Columnar and Mesoporous Thin Films: Evidence, Scrutiny and Limitations for Infrared Optics. *Appl. Surf. Sci.* **2019**, *493,* 807–817.

TOC GRAPHIC

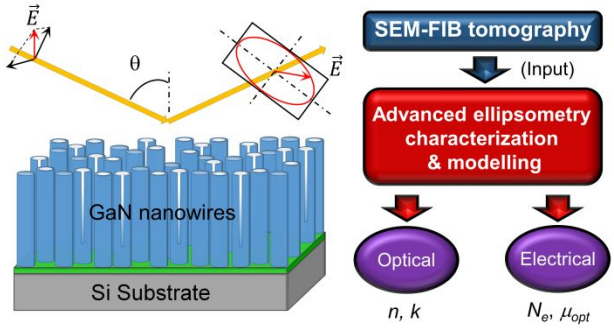
$\vec{E}$
θ
$\vec{E}$
GaN nanowires
Si Substrate
SEM-FIB tomography
(Input)
Advanced ellipsometry characterization & modelling
Optical
Electrical
n, k
N_e, μ_{opt}

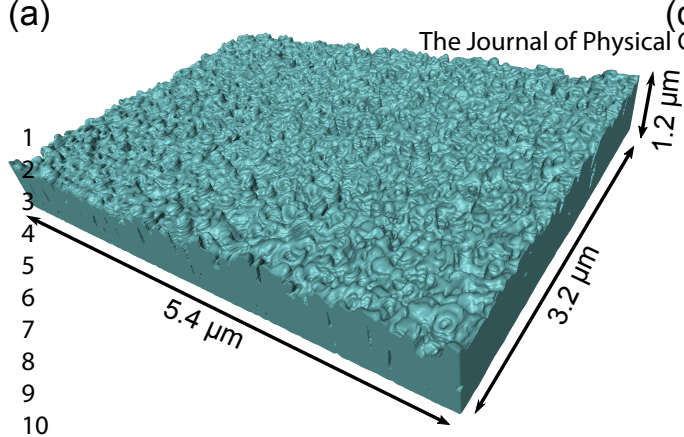

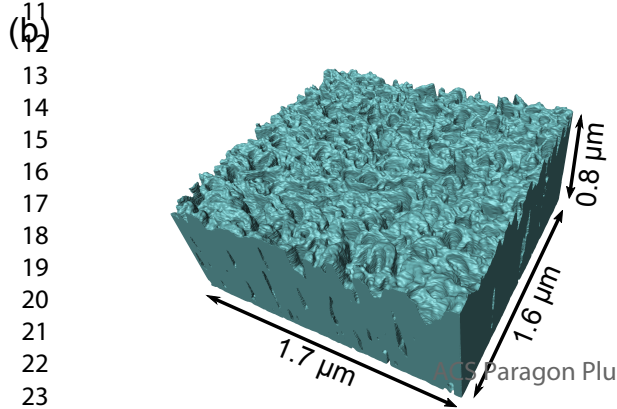

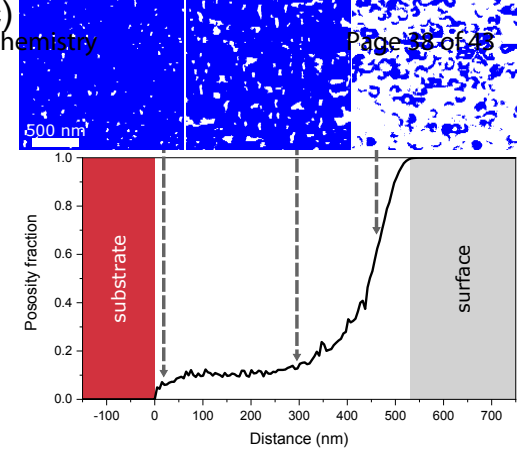

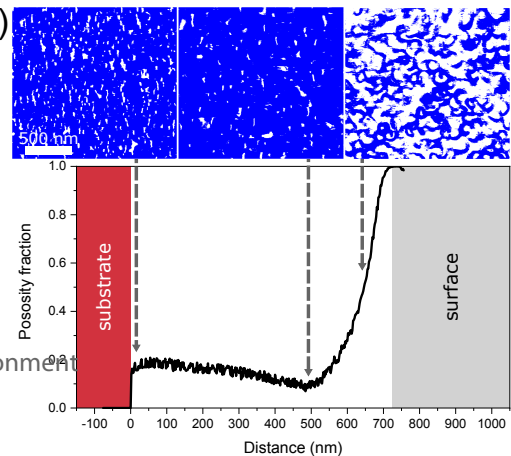

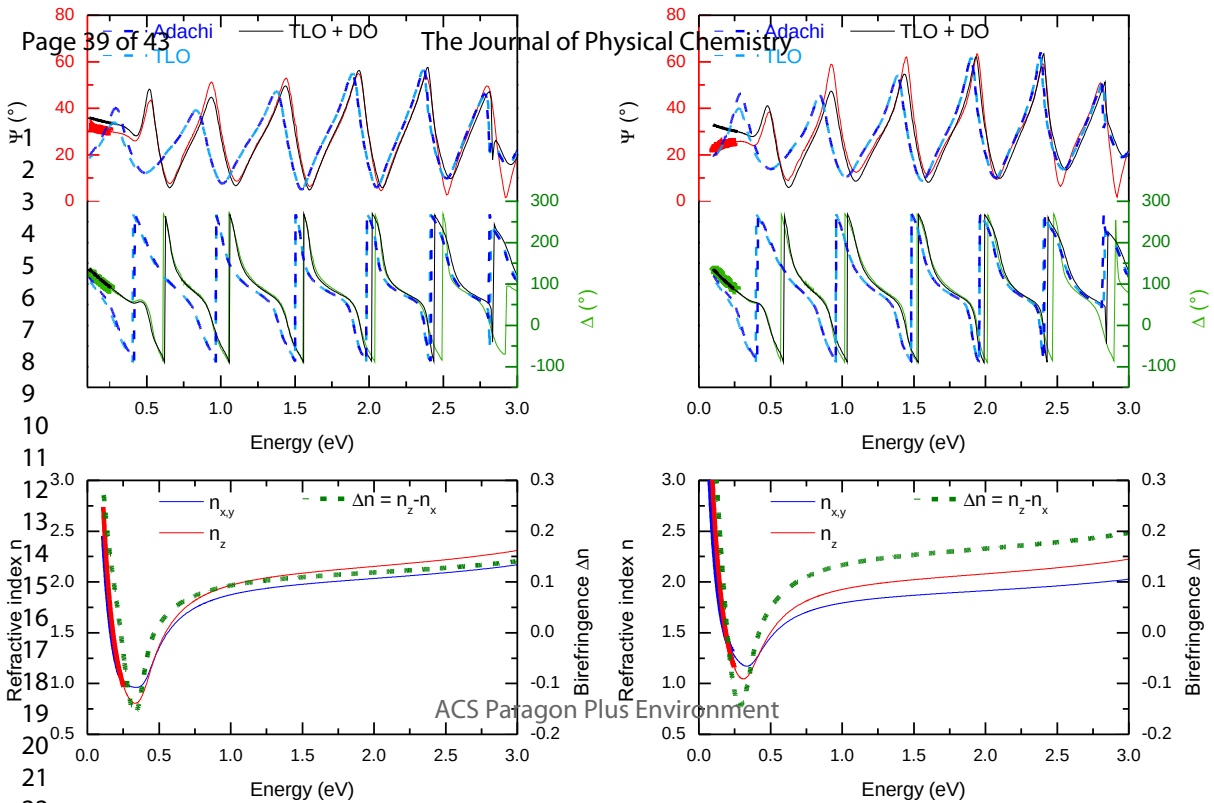

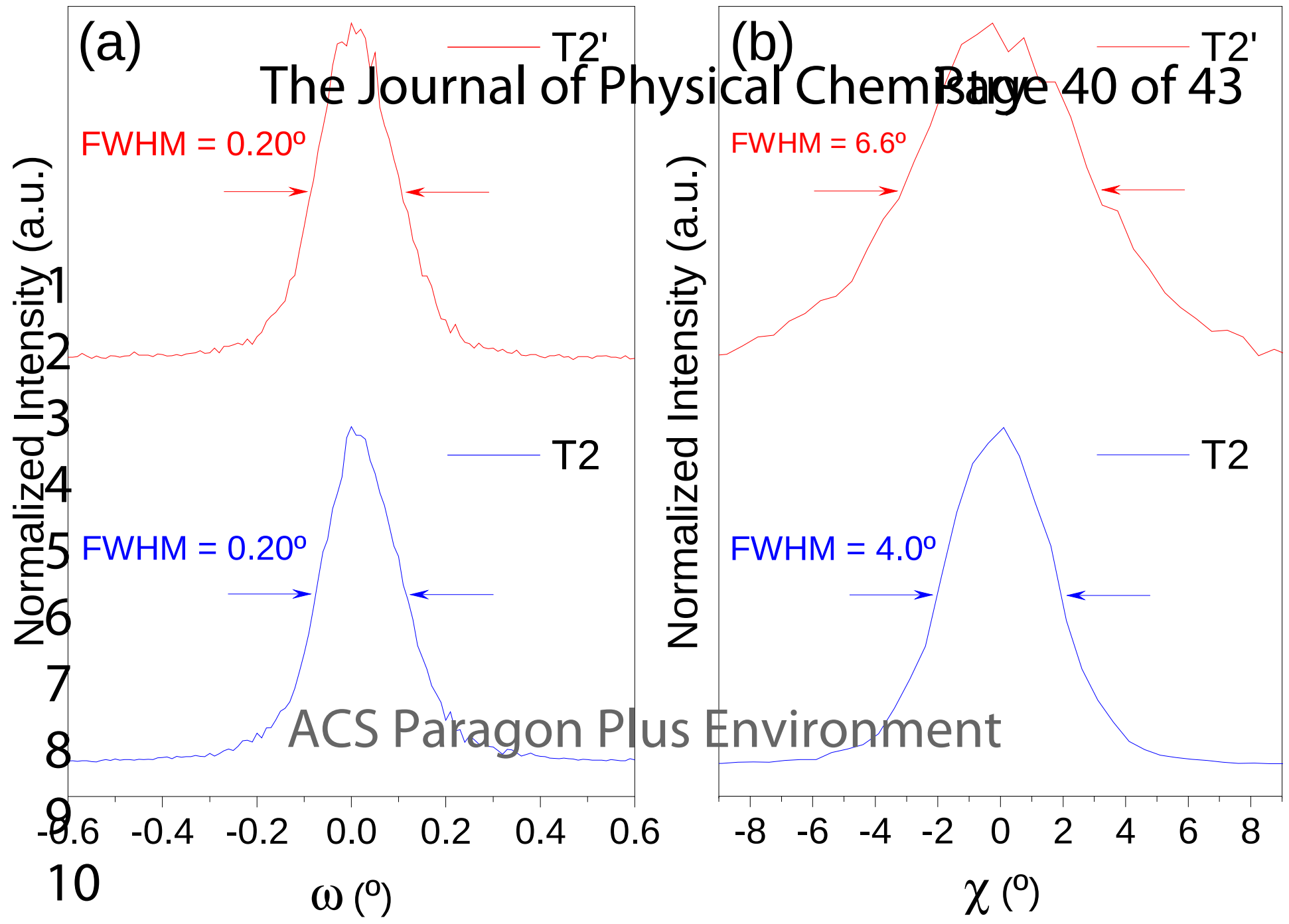

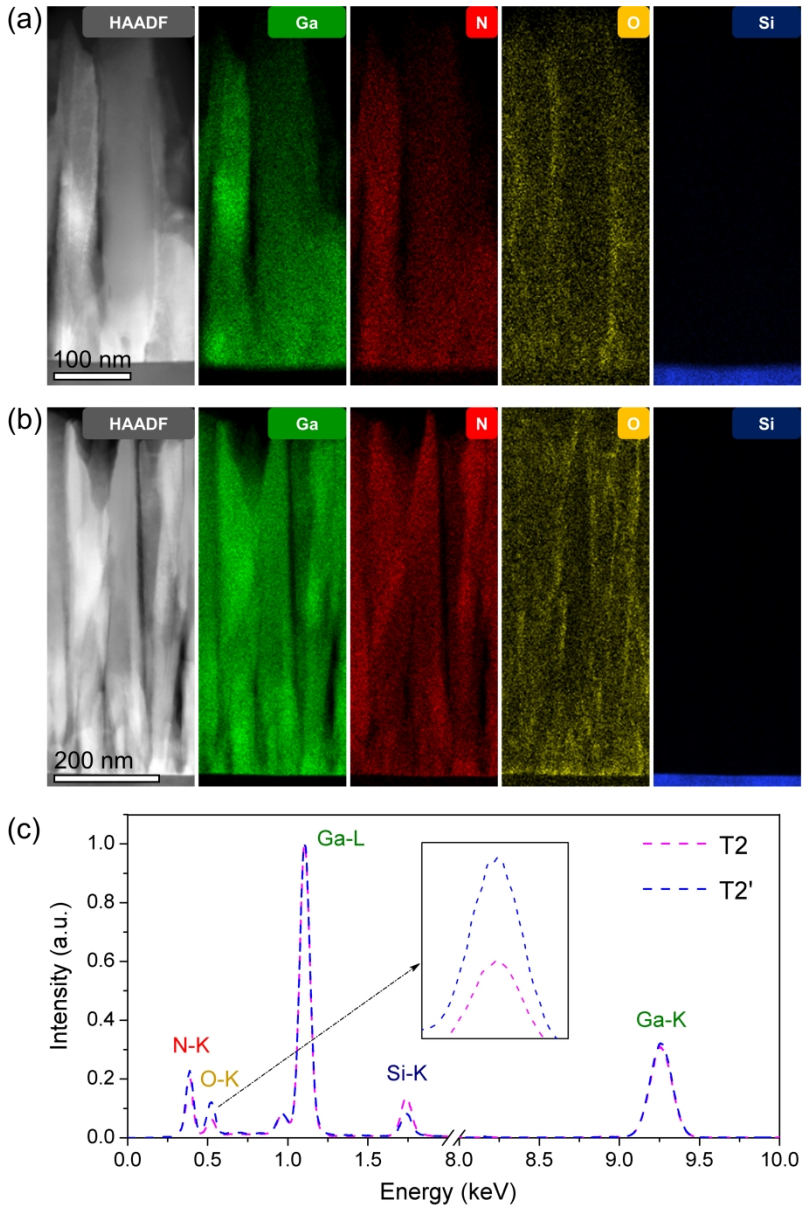

STEM-HAADF and EDX elemental maps of (a) T2 and (b) T2’ samples obtained for Ga, N, O and Si atoms. (c) EDX spectra, normalized at Ga-L_α peak (1098 eV), for T2 (magenta dashed line) and T2’ (blue dashed line) samples. The inset corresponds to the feature of the O-K_α peak (525 eV).

82x123mm (1000 x 1000 DPI)

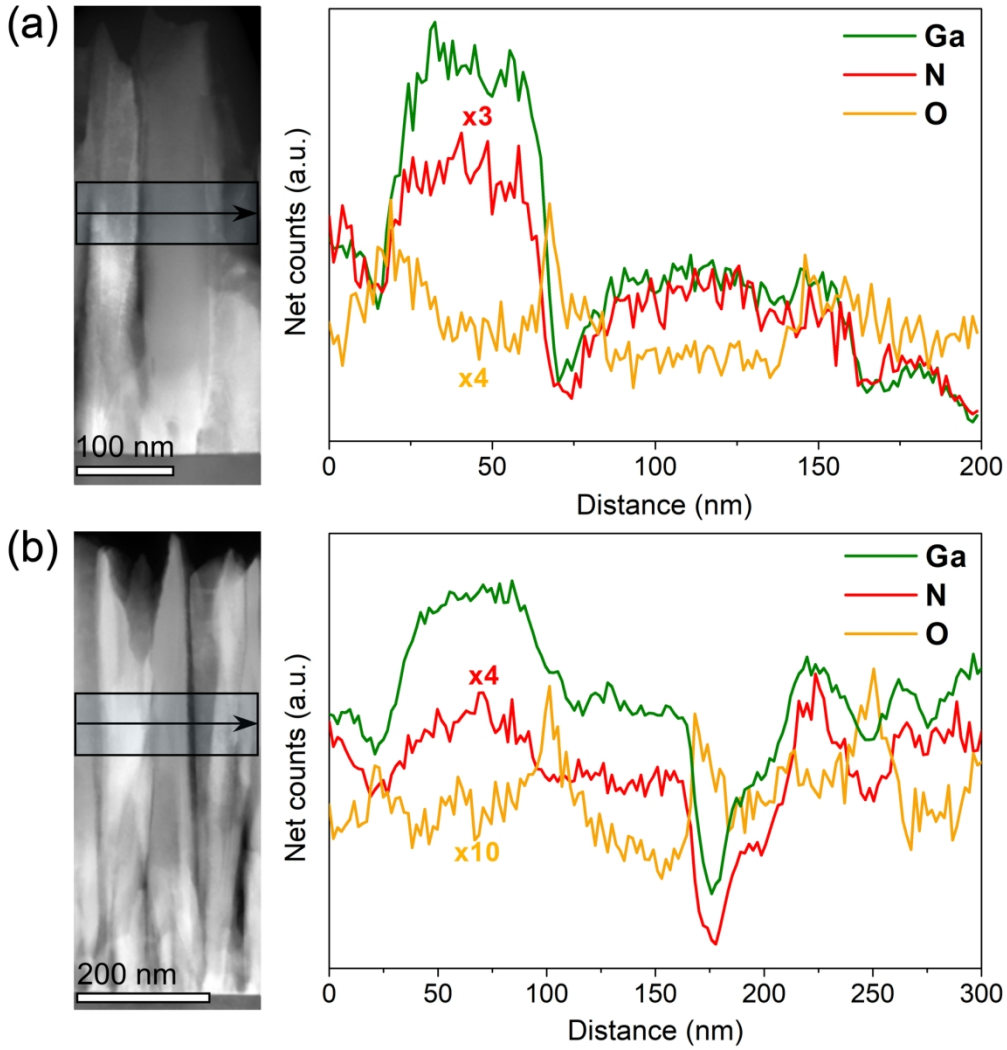

STEM-HAADF and Ga, N and O EDX elemental profiles for (a) T2 and (b) T2' samples. Note that such profiles were integrated across the NWs following the direction indicated by the arrows.

81x88mm (600 x 600 DPI)

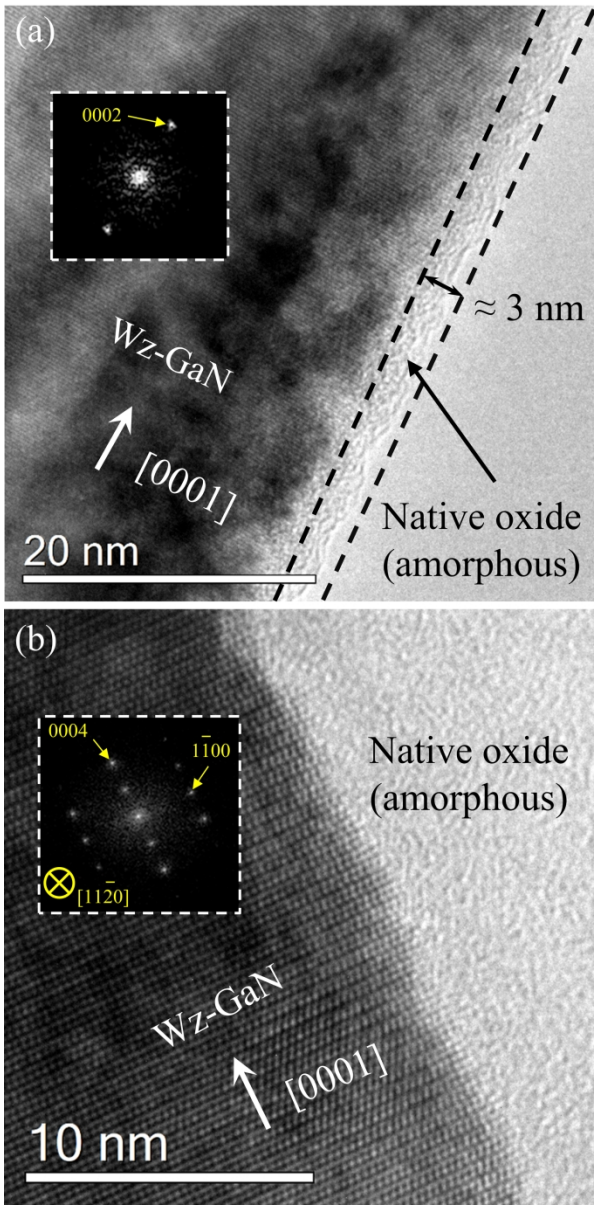

High-resolution TEM micrographs and corresponding FFT diffractions of single nanowires of (a) T2 and (b) T2′ samples. Note that these TEM observations were conducted on two FIB lamellae prepared by using the same SEM-FIB systems as for FIB tomography experiments.

79x162mm (600 x 600 DPI)